Transient simulations of a resonant tunneling diode

Olivier Pinaud

View Online   Export Citation

ARTICLES YOU MAY BE INTERESTED IN

Transient simulations of a resonant tunneling diode

Olivier Pinaud[a)]

Mathématiques pour l'industrie et la Physique, Unité mixte de recherche 5640 (CNRS), Université Paul Sabatier 118, route de Narbonne, 31062 Toulouse Cedex, France

Stationary and transient simulations of a resonant tunneling diode in the ballistic regime are presented. The simulated model consists in a set of Schrödinger equations for the wave functions coupled to the Poisson equation for the electrostatic interaction. The Schrödinger equations are applied with open boundary conditions that model continuous injection of electrons from reservoirs. Automatic resonance detection enables reduction of the number of Schrödinger equations to be solved. A Gummel type scheme is used to treat the Schrödinger–Poisson coupling in order to accelerate the convergence. Stationary $I-V$ characteristics are computed and the transient regime between two stationary states is simulated. © *2002 American Institute of Physics.*
[DOI: 10.1063/1.1494127]

I. INTRODUCTION

The resonant tunneling diode (RTD) is now among the most studied quantum devices both at the theoretical and experimental level.[1–4] An accurate simulation of such a device, a prototype of a one-dimensional quantum device, is of primary importance to develop reliable design tools. The RTD structure is treated as an open system and is generally partitioned into two large reservoirs and an active region. The reservoirs model the exchange of electrons with the external electrical circuit. The active region consists in a single quantum well, bounded by barriers. All important physical effects such as tunneling or scattering, take place in this small region. The calculations should therefore be performed only within the short device domain. This implies the derivation of realistic boundary conditions (BC) modeling the continuous injection of electrons at the interface. In addition, the current flow through the device is mainly due to electrons having the resonant energies of the double barriers. Therefore, even in the ballistic regime, the RTD simulation entails several problems arising from the existence of resonances, the important Coulomb effects, and the interaction of particles with reservoirs. A reliable simulation thus requires:

(1) the design of some BCs at reservoir-active region interfaces and an accurate discretization of these BCs
(2) the detection of resonances that determine the $I-V$ characteristics
(3) an accurate and numerically "cheap" treatment of the Coulomb interaction.

Indeed, these three items contribute to the high nonlinearity of the device operation, which makes the simulation a delicate task.

Three equivalent approaches are proposed to model an RTD: the Wigner equation,[5,6] the nonequilibrium Green function theory,[7–9] and the Schrödinger equation approach.[10,11] The latter approach is adopted in this work:

electrons are assumed to be in a mixed state whose statistics are determined by the chemical potential of the access zones (treated as reservoirs). Each state is determined by solving a collisionless Schrödinger equation with open boundary conditions. The electrostatic interaction is taken into account at the Hartree level. The self-consistent effects can be also introduced in a less precise way using the Thomas–Fermi approximation.[12–14] Many theoretical approaches have been proposed to incorporate particle scattering in quantum transport simulation.[15–18] The inelastic scattering can be addressed at various levels of sophistication. The electron–phonon interaction is often treated within the single electron approximation and a truncation of self-consistent Born expansion.[17–19] Stationary scattering models have successfully predicted the collision dominated regime[20,21] but do not handle the collisionless regime. A related approach is based on the Pauli master equation.[22,23] The ballistic approach, compared to models including collisions, provides fast simulation tools and quite realistic results. The peak location is predicted quite precisely and the shape of the $I-V$ characteristics is comparable with that of a real device. The main drawback of the ballistic approach is the overestimation of the peak-to-valley ratio because the valley current is dominated by scattering effects.

The outline of the paper is as follows: Sec. II is devoted to the introduction of the mathematical model both in the stationary and time-dependent cases. Special attention is given to boundary conditions. In Sec. III, the numerical methods are presented. They deal with the discretization of the BCs, the automatic detection of resonances in the stationary case, and the Coulomb coupling. In Sec. IV, the numerical results for an GaAs–AlGaAs type structure both in the stationary case ($I-V$ curves) and in the transient regime between two stationary states are presented.

II. THE MODEL

A. The stationary regime

The double-barrier heterostructure[24] extends over in the interval $[a,b]$ (Fig. 1) and the transport is assumed to be one

---
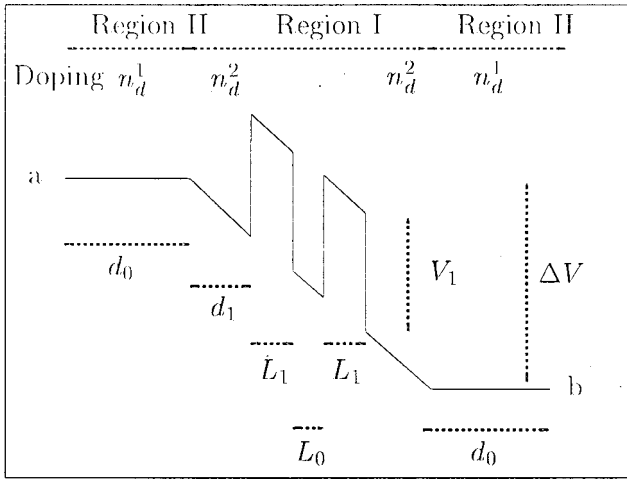[a)]Electronic mail: pinaud@mip.ups-tsle.fr

FIG. 1. Schematic drawing of a resonant tunneling structure under bias. Region I is the device region while region II represent a small part of the access zones. The region II is coupled with the exterior domain thanks to transparent boundary conditions and the space-charge effects are assumed to hold only in region I and II.

dimensional (the wave functions in the parallel directions to the barriers are plane waves). The contacts a and b are linked to electron reservoirs at thermal equilibrium, injecting electrons with some given profiles $g_a(p)$, $p \geq 0$, $g_b(p)$, $p \leq 0$, where p is the momentum of the injected electron (typically, the profiles g_a and g_b correspond to Fermi–Dirac statistics). The region $[a,b]$ contains the double barriers, the eventual spacers (region I on Fig. 1), and a small part of highly doped access regions where electroneutrality occurs (region II on Fig. 1). At negative times, the electrostatic potential is assumed to be constant in the leads, equal to V_a^- at the source contact a and V_b^- at the drain contact b. The electron–electron interaction at Hartree level is taken into account by solving a Poisson equation in $[a,b]$.

For the electrons injected at $x=a$ with momentum $p \geq 0$, the wave function ψ_p satisfies a stationary effective-mass Schrödinger equation with open boundary conditions. These boundary conditions are obtained by explicitly solving the Schrödinger equation in the reservoirs and by assuming the continuity of the wave function and its derivative at the interfaces. Thanks to these BCs, the problem is solved in the bounded domain $[a,b]$[25] and not on an infinite domain:

$$-\frac{\hbar^2}{2m}\psi_p'' - eV^-\psi_p = E_p^a\psi_p, \quad (p \geq 0),$$

$$\hbar\psi_p'(a) + ip\psi_p(a) = 2ip, \quad \hbar\psi_p'(b) = ip_b\psi_p(b), \tag{1}$$

where $\hbar$ is the reduced Planck constant, m is the effective mass of the electron, assumed to be constant along the device, and V^- is the total electrostatic potential in the device. In the same way, electrons injected at $x=b$ with momentum $p \leq 0$ are represented by the wave function ψ_p satisfying the Poisson equation,

$$-\frac{\hbar^2}{2m}\psi_p'' - eV^-\psi_p = E_p^b\psi_p, \quad (p \leq 0),$$

$$\hbar\psi_p'(b) + ip\psi_p(b) = 2ip, \quad \hbar\psi_p'(a) = ip_a\psi_p(a), \tag{2}$$

where

$$p_b = \sqrt{p^2 + 2em(V_b^- - V_a^-)},$$

$$p_a = \sqrt{p^2 + 2em(V_a^- - V_b^-)},$$

$$E_p^a = \frac{p^2}{2m} - eV_a^-, \quad E_p^b = \frac{p^2}{2m} - eV_b^-.$$

$\sqrt{\alpha}$ is the complex square root of the real number α having a positive real part ($\alpha \geq 0$) or positive imaginary part ($\alpha \leq 0$). Since it is assumed that $V^- = V_a^-$ for $x < a$ and V_b^- for $x > b$, then for $p > 0$, the waves functions are plane waves,

$$\psi_p(x) = e^{-ip(x-a)/\hbar} + r_p e^{ip(x-a)/\hbar}, \quad (x < a),$$

$$\psi_p(x) = t_p e^{ip_b(x-b)/\hbar}, \quad (x > b), \tag{3}$$

and for $p < 0$

$$\psi_p(x) = e^{ip(x-b)/\hbar} + r_p e^{-ip(x-b)/\hbar}, \quad (x > b),$$

$$\psi_p(x) = t_p e^{ip_a(x-a)/\hbar}, \quad (x < a), \tag{4}$$

where r_p and t_p are not prescribed coefficients but deduced from the solution. The transmission coefficients can be computed as

$$p > 0 \quad T(p) = \frac{\sqrt{[p^2 + 2em(V_b^- - V_a^-)]^+}}{|p|}|t_p|^2, \tag{5}$$

$$p < 0 \quad T(p) = \frac{\sqrt{[p^2 - 2em(V_b^- - V_a^-)]^+}}{|p|}|t_p|^2, \tag{6}$$

where $(a)^+ = \max(a,0)$. Since the electrons are assumed to be in a mixed state, the electronic density is

$$n(x) = \int_{-\infty}^{+\infty} g(p)|\psi_p(x)|^2 dp, \tag{7}$$

where $g(p) = g_a(p)$ for $p > 0$, $g(p) = g_b(b)$ for $p < 0$, and g_a, g_b are the statistics of the electrons injected at $x=a$ and $x=b$, respectively; typically, g_a and g_b are Fermi–Dirac statistics.

The electrostatic potential V^- is split into two parts: $V^- = V_e^- + V_s^-$, where V_e^- is the external potential (including double barriers, applied voltage) and V_s^- is the self-consistent potential satisfying

$$\frac{d^2V_s^-}{dx^2}(x) = \frac{e}{\varepsilon}[n(x) - n_D(x)],$$

$$V_s^-(a) = V_s^-(b) = 0, \tag{8}$$

where ε is the dielectric constant, and n_D the doping density. The one dimensional Fermi statistics is given by

$$g(p) = \frac{mk_bT}{2\pi^2}\log\left\{1 + \exp\left[\left(-\frac{p^2}{2m} + E_F\right)\bigg/ k_bT\right]\right\}, \tag{9}$$

where k_b is the Boltzmann constant, T the temperature, and E_F the Fermi level. The current is defined by

$$J(x) = J = \frac{e\hbar}{m}\int_{-\infty}^{+\infty} g(p)\mathfrak{J}(\overline{\psi_p}\psi_p')dp, \tag{10}$$

where $\mathfrak{J}$ denotes the imaginary part. By using the boundary conditions of Eqs. (1), (2) and (5), (6), J reads

$$J = \frac{e}{m} \int_0^\infty [g_a(p) - g_b(p)] p T(p) dp. \tag{11}$$

The time-dependent model is now presented.

B. The time-dependent regime

After the stationary regime is computed, the external potentials are switched at time $t=0$ to V_a^+ and V_b^+ (without loss of generality, it is assumed that $V_a^- = V_a^+$). Hence, the external potential changes accordingly from V_e^- to V_e^+. It can also be assumed that the electrostatic interaction takes place in the device $[a,b]$, while the electrostatic potential remains stationary at the contacts. Therefore, the total electrostatic potential is

$$V(t,x) = V_e^+(x) + V_s^+(t,x), \tag{12}$$

$$V_s^+(t,a) = V_s^+(t,b) = 0, \quad \frac{d^2V_s^+}{dx^2} = \frac{e}{\varepsilon}(n - n_D), \tag{13}$$

where the density $n(t,x)$ is defined by

$$n(t,x) = \int_{-\infty}^{+\infty} g(p)|\psi_p(t,x)|^2 dp, \quad x \in [a,b], \tag{14}$$

and the wave functions ψ_p are solutions of

$$i\hbar \frac{d\psi_p}{dt} = -\frac{\hbar^2}{2m} \frac{d^2\psi_p}{dx^2} - eV\psi_p, \quad (x \in [a,b]),$$

$$\psi_p(0,x) = \psi_p^-(x), \tag{15}$$

and ψ_p^- are the stationary wave functions associated with the potential V^- [solutions of Eqs. (1) and (2)]. As in the stationary case, the single-electron wave function ψ_p satisfies nonhomogeneous open boundary conditions[26–28] modeling the interaction with the reservoirs. They read:

$$\frac{d\psi_p}{dx}(a,t) - \frac{d\psi_p^-}{dx}(a)e^{-i(E_p^+ t/\hbar)}$$

$$= \mathscr{D}_{1/2}^a[\psi_p(a,.) - \psi_p^-(a)e^{-i(E_p^+ \hbar)}], \tag{16}$$

$$\frac{d\psi_p}{dx}(b,t) - \frac{d\psi_p^-}{dx}(b)e^{-i(E_p^- t/\hbar)}$$

$$= \mathscr{D}_{1/2}^b[\psi_p(b,.) - \psi_p^-(b)e^{-i(E_p^- \hbar)}], \tag{17}$$

with

$$\mathscr{D}_{1/2}^\alpha[f(.)]$$

$$= \sqrt{\frac{2m}{\pi\hbar}}e^{-(\pi/4)i}e^{i(eV^\alpha t/\hbar)}\frac{d}{dt}\int_0^t \frac{f(\tau)e^{-i(eV^\alpha \tau/\hbar)}}{\sqrt{t-\tau}}d\tau,$$

$$V^\alpha = \begin{cases} V_a^- & \text{if} \quad \alpha=a \\ V_b^+ & \text{if} \quad \alpha=b \end{cases}, \quad E_p^+ = \begin{cases} E_p^a & \text{if} \quad p>0 \\ E_p^b & \text{if} \quad p<0, \end{cases}$$

$$E_p^- = \begin{cases} E_p^a - e(V_b^+ - V_b^-) & \text{if} \quad p>0 \\ E_p^b - e(V_b^+ - V_b^-) & \text{if} \quad p<0. \end{cases}$$

III. NUMERICAL METHODS

A. Position of the problem

The space-charge effects imply that the system of equations (1)-(2)-(7)-(8) is highly nonlinear. Indeed, the Wentzel–Kramers–Brillouin approximation indicates that the density n depends exponentially on the self-consistent potential V_s^-. Subsequently, the natural iterating algorithm given by

$$n(V_s^{old})(x) = \int_{-\infty}^{+\infty} g(p)|\psi_p(V_s^{old})(x)|^2 dp,$$

$$\frac{d^2V_s^{new}}{dx^2}(x) = \frac{e}{\varepsilon}[n(V_s^{old})(x) - n_D(x)],$$

fails to converge for any initial guess. Typically, an oscillating regime is observed: a high density generates a high potential, which decreases the density and therefore the potential. Then, this low potential increases the density and so on.

A possible solution is to use a relaxation algorithm which reads

$$n(V_s^{old})(x) = \int_{-\infty}^{+\infty} g(p)|\psi_p(V_s^{old})(x)|^2 dp,$$

$$\frac{d^2V_s^*}{dx^2}(x) = \frac{e}{\varepsilon}[n(V_s^{old})(x) - n_D(x)],$$

$$V_s^{new} = \alpha V_s^* + (1-\alpha)V_s^{old}, \quad \alpha \ll 1.$$

The convergence toward a solution is very slow because of the small size of the parameter α (typically <0.05). Thus, to accelerate the convergence rate, a self-consistent scheme inspired from the one introduced by Gummel[29] for steady state transistor calculation is used.

Another difficulty lies in the computation of the electronic density n. Indeed, the current is mainly generated by the transmitted electrons, that is to say electrons that are in the resonant states of the double barriers. If the barriers are wide or high, the resonant peaks are sharp and their widths are very small (see Fig. 7). Therefore, to take the resonant states into account, the mesh size in the momentum variable p must be very small. This implies solving a huge number of Schrödinger equations and thus prohibitively increasing the numerical cost. The proposed solution is based on an adaptive mesh size, using the logarithmic derivative of the transmission coefficient. The mesh will be refined only at the resonance regions, which results in a reduction of the computational cost.

B. The stationary regime

1. The linear equations

The system (1) is solved just like any ordinary differential equation of the first order on a function u_p using a Runge–Kutta algorithm with boundary conditions $\hbar u_p'(b)$

1990   J. Appl. Phys., Vol. 92, No. 4, 15 August 2002

O. Pinaud

$=ip_b$ and $u_p(b)=1$. The equations are linear and it suffices to normalize u_p by $2ip/[\hbar u'_p(a)+ipu_p(a)]$ to recover ψ_p. The negative momentum case is treated analogously.

2. The Gummel method

In classical transport models, the Fermi–Dirac statistics are approximated by the Boltzmann statistics, and the expression of carrier concentrations yields an exponential dependence on the electrostatic potential. Hence, the exponential behavior is explicitly included in the definition of the electronic density, which can be written $n(V) = \exp(V/V_{\text{ref}})f(V)$. Integrating this fact in the Poisson equation (8) leads to a modified Schrödinger–Poisson system solved with the following algorithm:

$$\frac{d^2V_s^{\text{new}}}{dx^2}=\frac{e}{\varepsilon}\left[f(V_s^{\text{old}})\exp\frac{(V_s^{\text{new}}+V_e^-)}{V_{\text{ref}}}-n_D\right].$$

The quantity $f(V_s^{\text{old}})$ being equal to $\exp[-(V_s^{\text{old}}+V_e^-)/V_{\text{ref}}]n(V_s^{\text{old}})$, the Gummel method reads:

$$\frac{d^2V_s^{\text{new}}}{dx^2}=\frac{e}{\varepsilon}\left[n(V_s^{\text{old}})\exp\frac{(V_s^{\text{new}}-V_s^{\text{old}})}{V_{\text{ref}}}-n_D\right]. \quad (18)$$

This nonlinear equation is solved using a Newton algorithm, and the convergence toward a solution is much faster than the relaxation algorithm. The potential reference V_{ref} is adjusted to decrease the number of iterations. The linear version of the Gummel method is obtained by a Taylor expansion of Eq. (18), that is,

$$\frac{d^2V_s^{\text{new}}}{dx^2}-\frac{en(V_s^{\text{old}})}{\varepsilon V_{\text{ref}}}V_s^{\text{new}}=\frac{e}{\varepsilon}\left[n(V_s^{\text{old}})\left(1-\frac{V_s^{\text{old}}}{V_{\text{ref}}}\right)-n_D\right]. \quad (19)$$

3. The adaptive momentum mesh size method

The main task, to obtain a fine mesh only at the resonance regions, is done by detecting the transmission peaks. One way to detect these resonant energies is to use the logarithmic derivative of the transmission coefficient. It reads (for the positive momentum case)

$$\frac{d\log T}{dp}=-\frac{1}{p}+\frac{p}{p_b^2}+\frac{2}{|\psi_p(b)|^2}\Re\left[\overline{\psi_p}(b)\frac{\partial\psi_p}{\partial p}(b)\right], \quad (20)$$

where $\Re$ denotes the real part. The logarithmic derivative is necessary because the resonances are too thin to be detected by the usual derivative. Typically, the transmission coefficient profile corresponding to a resonant energy is, without logarithmic scaling, a vertical line. Hence, when $|d\log T/dp|$ is less than a given threshold, the mesh size is large, whereas if $|d\log T/dp|$ is above this threshold, the mesh size is refined.

C. The time-dependent regime

To discretize Eq. (15), a finite difference Crank–Nicholson scheme is used. With uniform grid points $x_j=j\Delta x(0\leq j\leq J)$, $t_n=n\Delta t$ and the approximation $\psi_j^n\approx\psi(x_j,t_n)$, this scheme reads

$$r(\psi_j^{n+1}-\psi_j^n)=\psi_{j+1}^{n+1}-2\psi_j^{n+1}+\psi_{j-1}^{n+1}+\psi_{j+1}^n-2\psi_j^n$$
$$+\psi_{j-1}^n+wV_j^{n+1/2}(\psi_j^{n+1}+\psi_j^n), \quad (21)$$

with

$$r=-\frac{4im\Delta x^2}{\hbar\Delta t}, \quad w=\frac{2me\Delta x^2}{\hbar^2}, \quad V_j^{n+1/2}=V(t_{n+\frac{1}{2}},x_j).$$

The boundary conditions (16)–(17) are discretized following the scheme of Ref. 28, i.e., $(n\geq1)$:

$$\psi_1^n=\sigma_0^{-n}\sum_{k=0}^n\sigma_0^k\psi_0^kl_{n-k}, \quad \psi_{J-1}^n=\sigma_J^{-n}\sum_{k=0}^n\sigma_J^k\psi_J^kl_{n-k}, \quad (22)$$

with

$$l_n=\left(1+i\frac{\rho}{2}\right)\delta_n^0-i\rho(-1)^n+i\sqrt[4]{\rho^4+16\rho^2}e^{-i(\theta/2)}$$
$$\times\left[\frac{1}{2}e^{-i\theta}f_n-\mu\sum_{k=0}^n(-1)^{n-k}f_k\right],$$

$$\rho=\frac{4m\Delta x^2}{\hbar\Delta t}, \quad \theta=\arctan\frac{4}{\rho}, \quad \mu=\frac{\rho}{\sqrt{\rho^2+16}},$$

$$\sigma_0=\frac{1-(\Delta tV_a^+/2i\hbar)}{1+(\Delta tV_a^+/2i\hbar)}, \quad \sigma_L=\frac{1-(\Delta tV_b^+/2i\hbar)}{1+(\Delta tV_b^+/2i\hbar)},$$

$$f_0=1, \quad f_n=e^{-in\theta}P_n(\mu)-e^{-i(n-1)\theta}P_{n-1}(\mu),$$

where P_n is the Legendre polynomial of order n. This discretization has the advantage of preserving the unconditional stability of the Crank–Nicholson scheme.

The evolution of the self-consistent potential V_s (the sign $+$ is dropped) is computed using a classical scheme for nonlinear Schrödinger equations which reads

$$V_s^{n+3/2}=2V_*^{n+1}-V_s^{n+1/2}$$

where V_*^{n+1} is the solution of the discretized Poisson equation at time t_{n+1}.

IV. RESULTS

A. Parameters

The barriers, separated by a 5 nm quantum well, are 5 nm wide and 0.3 eV high. Two zones are distinguished: the first is the double-barrier zone (region I on Fig. 1), 35 nm wide, including a spacer layer of 10 nm doped at 5×10^{15} cm^{-3} on each side. The second zone (region II on Fig. 1) corresponds to the access zones, each 50 nm long, doped at 10^{18} cm^{-3}, placed adjacent to the first zone. The boundary conditions are applied at the edge of the second zone. The effective mass is constant in the whole device and equal to $0.067m_e$. The relative permittivity ε_r is 11.44. For numerical computation, the wave functions are parametrized by the wave vector $k=p/\hbar$ rather than with the momentum p. The Gummel and relaxation algorithms are stopped when the relative error on the potential between two iterations is less than a predefined threshold.
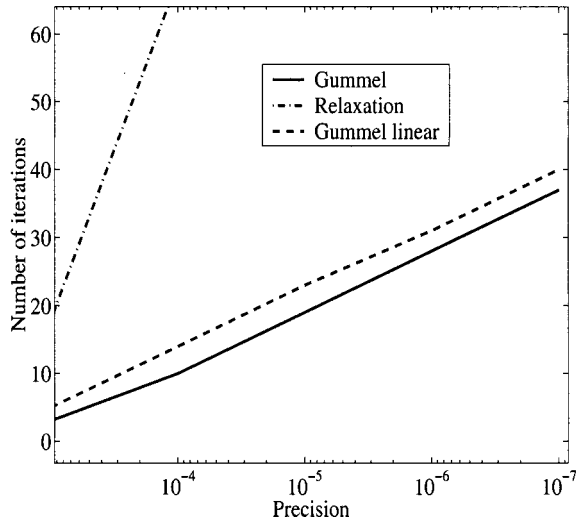
FIG. 2. Comparison of the effectiveness of the methods used for the Poisson coupling: number of iteration vs precision for a bias of 0.05 V. The solid line represents the Gummel method, the dashed line the linear Gummel method, and the dash-dot line, the relaxation.

n_d^1	n_d^2	L_0	L_1	d_0
10^{18} cm^{-3}	5.10^{15} cm^{-3}	5 nm	5 nm	50 nm

d_1	m_{eff}	ε_r	T	V_{ref}	V_1
10 nm	$0.067m_e$	11.44	300 K	0.03 V	-0.3 V

B. Effectiveness of the methods

In the absence of polarization (i.e., $V_a^- = V_b^- = 0$ V), it is observed that the Gummel algorithm converges in the stationary case with zero as an initial guess for the self-consistent potential. In this case, the obtained potential is used to initialize the algorithm when the applied bias is not zero.

If a uniform grid used for momentum is precise enough to collect the resonances, there are around 2500 Schrödinger equations to solve. The adaptive mesh size algorithm decreases this number to around 400 for a light bias (less than 0.1 V) and to around 800 for a higher bias. The latter number is higher because a second well appears in front of the first barrier. Therefore the time cost is divided approximately by a factor of 6 for the first case and by a factor of 3 for the second case. Of course, if the barriers are thinner, the resonance peaks are wider and the improvement of the method is not as important. As far as the Gummel method (GM) is concerned, it is very efficient compared to the relaxation algorithm (RA) (see Fig. 2). Indeed, the threshold is reached in a few iterations with the GM, even if the prescribed precision is very high. Moreover, the RA needs a large number of iterations to converge up to a precision of 0.001. It can also be noted than the GM is slightly faster than the linear GM.

C. The stationary regime

Figures 3, 4, and 5 represent the density and the total potential for an applied bias of 0.1, 0.2, and 0.22 V, respectively. A bias of 0.2 V is associated with the current peak value and 0.22 V with the valley value. The spatial size step used for this computation is 0.27 nm, that is, a grid of 500
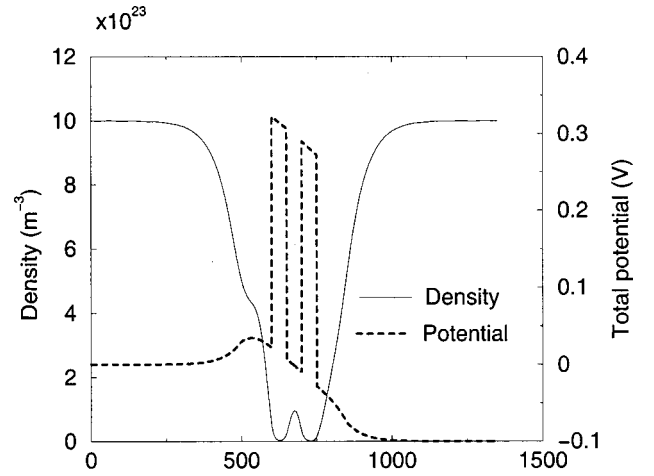

FIG. 3. Electronic density and Poisson potential plotted for an applied bias of 0.1 V. The solid lines is the potential and the dashed line, the density.

points. This latter number can be decreased to 200 if the bias is less than around 1.5 V. Up to this value of bias, the spatial mesh size must be refined because the electron wave length becomes smaller. Not all the wave functions have a significant contribution. In particular, the wave functions of the large energies weakly modify the electronic density. Indeed, these wave functions correspond to the occupation of high energy states, and the magnitude of these high energies may be estimated by the maximum occupied energy levels. The chosen maximal energy is around the Fermi level plus a few times k_bT. This gives a domain of integration for the density from 0 to $k_{max} = \sqrt{k_{Fermi}^2 + 7*2m_{eff}k_bT/\hbar^2}$. The threshold of the adaptive size step method is 1200 Å, the minimal size step is 5×10^{-5} Å^{-1} and the maximal 10^{-3} Å^{-1}.

In the regions where the total potential is zero, the electronic density is given by the donor density. This regime is called electroneutrality and precisely shows up on Figs. 3, 4, and 5 at the domain of the first spacers (region II).

Figure 6 shows the $I-V$ curves at 77 and 300 K for the nonlinear case, and at 300 K for the linear case. The self-
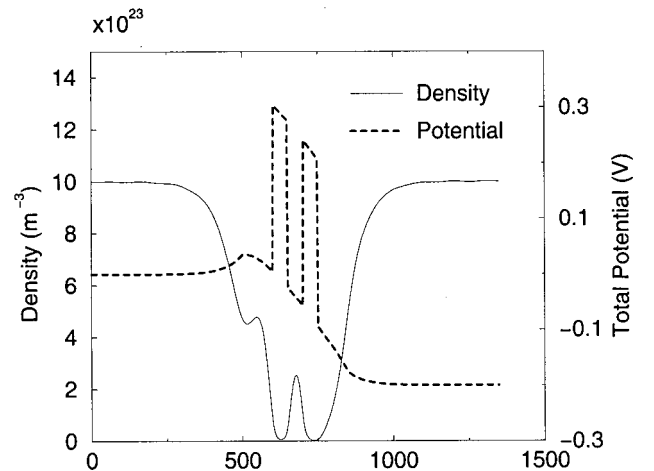

FIG. 4. Electronic density and Poisson potential plotted for an applied bias of 0.2 V, corresponding to the peak value. The density within the well is maximal. The solid line is the potential and the dash line, the density.
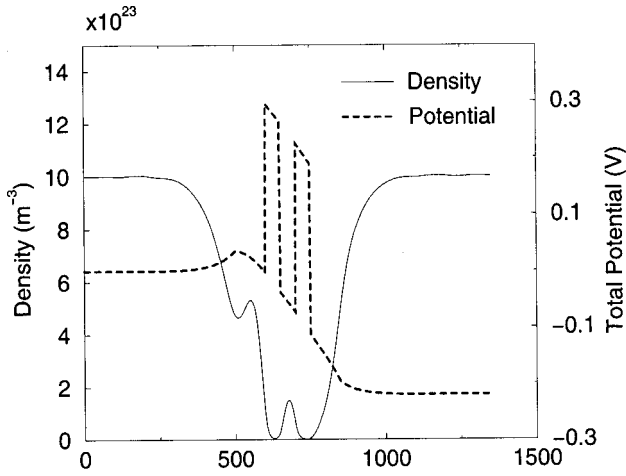
FIG. 5. Electronic density and Poisson potential plotted for an applied bias of 0.22 V, corresponding to the valley value. The density decreases to about a factor of 2 compared to a bias of 0.2 V. The solid line is the potential and the dash line, the density.

consistent potential pushes the peak to approximately 0.2 V, whereas the linear peak is about 0.15 V. This result is consistent with the decay of the density in the well observed in Fig. 5. It can be remarked that the ballistic approach is no longer valid in the valley. Indeed, in the valley the current is mainly due to the collisions process, to the electrons scattered down from their injected energy into the resonance. Therefore the peak-to-valley ratio is not as important as for a model with collisions.

Figure 7 represents the logarithm of transmission coefficient for two applied biases. The sharpness of the resonance peaks can be clearly observed.
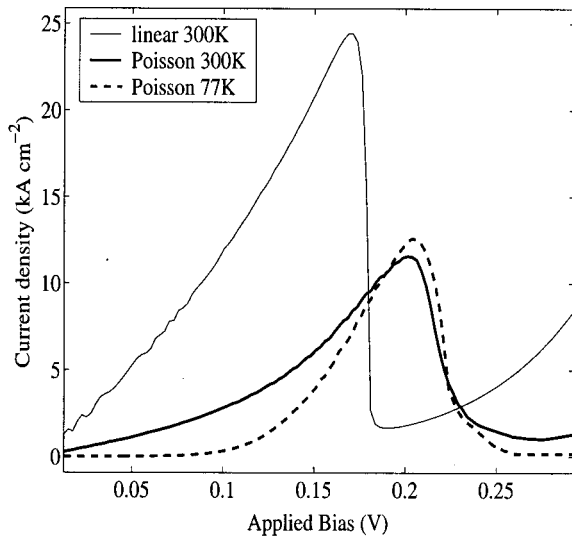

FIG. 6. $I–V$ curves. The solid and dash-dot lines represent the I curve of a model including self-consistent effects at 300 and 77 K, the dashed line represents a model without self-consistent effects at 300 K. The self-consistent effects push the peak to the value of 0.2 V and strongly decrease the peak current value.
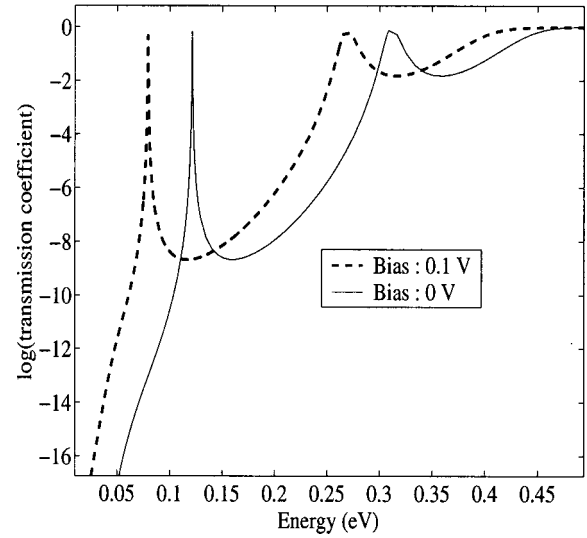

FIG. 7. Transmission coefficient in logarithmic scale for two different biases.

D. The time-dependent regime

The structure is the same as for the stationary model. The distance d_0 (see Fig. 1) is set to 10 nm, while retaining the same number of grid points as in the stationary model (500 points). Thus, the spatial size step becomes 0.11 nm. The main difficulty is the change of resonant energies when a bias is applied. Indeed, Fig. 7 clearly shows the shift of the peaks for two different biases. The chosen solution is to combine the momentum mesh corresponding to the initial bias with that of the final bias.

The size of the time step is set at 1 fs. A higher step size for time evolution would introduce strong reflections at the boundaries. Parallel computation using the message passing interface (MPI) is well suited to solve this kind of problem. Indeed, each processor solves a fixed quantity of Schrödinger equations independently and the results are collected by a single processor to compute the density and the Poisson potential. This method is not necessary for the stationary model because the time spent calculating is minimal.

Figures 8 and 9 represent the time evolution of the density and the current density for a shift of 0.1 V ($V_b^+ - V_b^- = 0.1$ V, $V_b^- = 0.1$ V). The current density exhibits an oscillatory behavior, while the electronic density seemingly does not. In fact, both quantities oscillate, but the amplitude of the oscillations is visible on the current and not on the density. Indeed, if the potential is lightly perturbated (for example a small shift of the applied bias), a first order perturbation analysis shows that the wave function is corrected with an oscillating term. Therefore, interferences are generated and the density and the current oscillate. In our case, the magnitude of the density is of order of the doping density. As the doping is very high, the magnitude of the oscillations is negligible compared to the high value of the electronic density. The situation is different for the current density. Indeed, the order of the final current is given by the difference between the two high values of the currents injected at each side of the device. Hence, the result of this difference between two high numbers has a very weak amplitude compared to that of
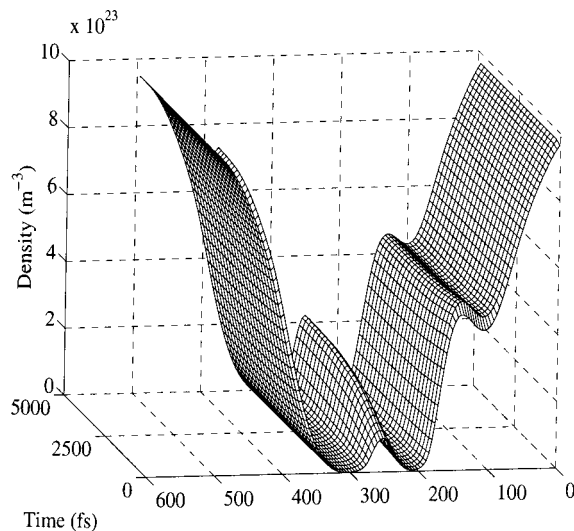
FIG. 8. Time evolution of the electronic density following a shift of 0.1 V of the applied bias. The initial condition is solution of the steady-state problem with an initial bias of 0.1 V. At positive times, the applied bias is moved to 0.2 V and the system evolves up to a stationary state. The density increases within the well up to a final value reached at about 5000 fs. The x-coordinate axis is reversed.

FIG. 10. Time evolution of the density at the middle of the well following two shifts of 0.1 V and 0.06 V. The initial condition is the solution of the steady-state problem with an initial bias of 0.1 V. The density is naturally bigger for a stronger shift. The solid line represents the density for a shift of 0.1 V and the dashed line, the density for a shift of 0.06 V.

the injected currents. Thus, the oscillations are not negligible. For example, a doping of 10^{18} cm^{-3} generates a current about 2000 kA/cm^2 while the $I–V$ curves (Fig. 6) shows a peak current around 15 kA/cm^2. The oscillations magnitude (see Figs. 11 and 9) are of the same order as that of the final current.

Figure 10 represents the evolution of the density at the middle of the well for two shifts, 0.1 and 0.06 V. Figure 11 shows the evolution of the spatial average of the current for three different shifts, 0.02, 0.06, and 0.1 V.

The current becomes almost homogeneous in space at approximately 300 fs (Figs. 9–11), while the density reaches

its final value at approximately 5000 fs (Figs. 8–10). The results are similar for different biases (Fig. 11). The main difference is the amplitude of the transition oscillations which increases with the bias. Of course, for thinner barriers the stationary solution is reached in a shorter period.

V. CONCLUSION

A model for ballistic transport in nanostructures, both in stationary and transient regime, has been presented. Simulations giving realistic results were performed with a nonprohibitive time cost. The last section shows that the adaptive mesh size method is very efficient and strongly reduces the numerical cost. The Gummel method really provides better
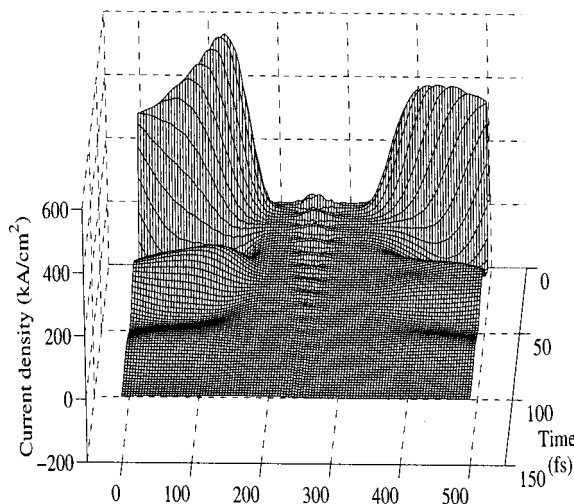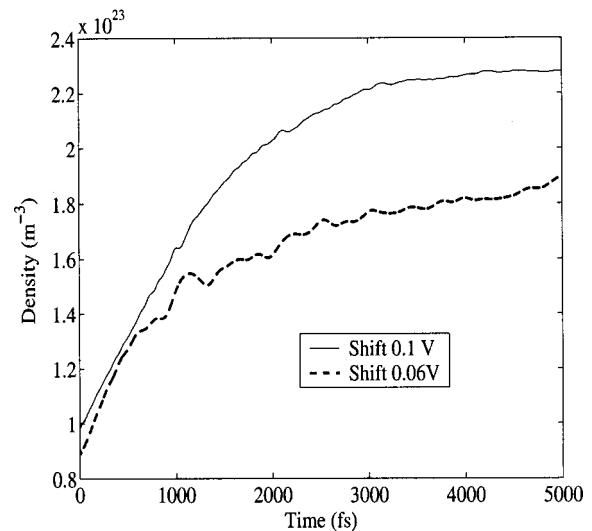

FIG. 9. Time evolution of the current density following a shift of 0.1 V of the applied bias. The initial condition is the solution of the steady-state problem with an initial bias of 0.1 V. At positive times, the applied bias is moved to 0.2 V and the system evolves up to a stationary state. The time axis is reversed.
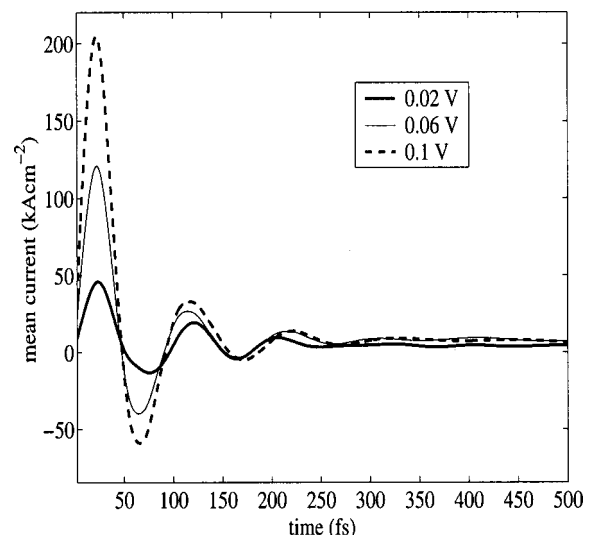

FIG. 11. Time evolution of the mean spatial current following three different shifts: solid line 0.06 V, dashed 0.1 V, dash-dot 0.02 V. The final value is reached at about 300 fs.

results than the relaxation algorithm. For the time dependent regime, the major problem is the smallness of the time step which implies a high number of iterations. A possible solution is to filter the oscillations that appear at the boundaries to increase the time step. Another improvement would be based on an adaptive integration over the momentum for the computation of the density in the transient regime. Indeed, as the potential varies in time, the energy position of resonances moves which requires a remeshing of the energy axis. In the present work, this idea was not developed and a static refined mesh determined by the positions of the initial and final resonances was used instead. This approach is, of course, not optimal. It induces an extra numerical cost which should be removed by the dynamical remeshing of the energy axis.

ACKNOWLEDGMENTS

[1] R. Tsu and L. Esaki, Appl. Phys. Lett. **22**, 562 (1973).
[2] B. Ricco and M. Y. Azbel, Phys. Rev. B **29**, 1970 (1984).
[3] D. K. Ferry and S. M. Goodnick (Cambridge University Press, Cambridge, UK, 1997).
[4] S. Datta (Cambridge University Press, Cambridge, UK, 1995).
[5] W. R. Frensley, Rev. Mod. Phys. **62**, 745 (1990).
[6] N. C. Kluksdahl, A. M. Kriman, D. K. Ferry, and C. Ringhofer, Phys. Rev. B **39**, 7720 (1989).
[7] R. C. Bowen, G. Klimeck, R. Lake, W. R. Frensley, and T. Moise, J. Appl. Phys. **81**, 3207 (1997).
[8] S. Datta, J. Phys.: Condens. Matter **2**, 8023 (1990).
[9] R. Lake, G. Klimeck, R. C. Bowen, and D. Jovanovic, J. Appl. Phys. **81**, 7845 (1997).
[10] M. Büttiker, Phys. Rev. Lett. **57**, 1761 (1986).
[11] R. Landauer, Philos. Mag. **21**, 863 (1970).
[12] T. B. Boykin, J. P. A. van der Wagt, and T. C. McGill, Phys. Rev. B **45**, 3583 (1992).
[13] P. Cheng and J. S. Harris, Appl. Phys. Lett. **55**, 572 (1989).
[14] M. A. Reed, W. R. Frensley, W. M. Duncan, R. J. Matyi, A. C. Seabaugh, and H. L. Tsai, Appl. Phys. Lett. **54**, 1256 (1989).
[15] F. A. Buot and K. L. Jensen, Phys. Rev. B **42**, 9429 (1990).
[16] B. C. Eu and K. Mao, Phys. Rev. E **50**, 4380 (1994).
[17] L. P. Kadanoff and G. Baym (Benjamin, Reading, MA, 1962).
[18] L. V. Keldysh, Zh. Eksp. Teor. Fiz. **47**, 1515 (1964) [Sov. Phys. JETP **20**, 1018 (1965)].
[19] R. Lake and S. Datta, Phys. Rev. B **45**, 6670 (1992).
[20] F. Chevoir and B. Vinter, Phys. Rev. B **47**, 7260 (1993).
[21] R. Ferreira and G. Bastard, Rep. Prog. Phys. **60**, 345 (1997).
[22] M. V. Fischetti, J. Appl. Phys. **83**, 270 (1998).
[23] W. Krech, A. Hädicke, and F. Seume, Phys. Rev. B **48**, 5230 (1993).
[24] B. Vinter and C. Weisbuch (Academic, New York, 1991).
[25] N. Ben Abdallah, P. Degond, and P. A. Markowich, Z. Angew. Math. Phys. **48**, 35 (1997).
[26] V. A. Baskakov and A. V. Popov, Wave Motion **14**, 123 (1991).
[27] B. Engquist and A. Majda, Math. Comput. **31**, 629 (1977).
[28] A. Arnold, VLSI Design **6**, 313 (1998).
[29] H. K. Gummel, IEEE Trans. Electron Devices **ED-11**, 455 (1964).